

1 **How does the air-sea coupling frequency affect**
2 **convection during the MJO passage?**

3 **Ning Zhao¹, Tomoe Nasuno¹**

4 ¹Japan Agency for Marine Earth Science and Technology, Yokosuka, Kanagawa, Japan

5 **Key Points:**

- 6 • High-frequency air-sea coupling improves the reproducibility of both convection
7 and upper ocean processes
8 • Low-frequency coupling causes phase-lagging in diurnal cycle
9 • Higher daytime SST is more important than the daily mean

Corresponding author: N. Zhao, zhaoning@jamstec.go.jp

Abstract

The importance of air-sea coupling in the simulation and prediction of the Madden-Julian Oscillation (MJO) has been well established. However, it remains unclear how air-sea coupling modulates the convection and related oceanic features on the subdaily scale. Based on a regional cloud-resolving coupled model, we evaluated the impact of the air-sea coupling on the convection during the active phase of the MJO by varying the coupling frequency. The model successfully reproduced the atmospheric and oceanic variations observed by satellite and *in situ* measurements but with some quantitative biases. According to the sensitivity experiments, we found that stronger convection was mainly caused by the higher sea surface temperatures (SSTs) generated in highly coupled experiments, especially when the coupling frequency was 1 hour or shorter. A lower coupling frequency would generate the phase lags in the diurnal cycle of SST and related turbulent heat fluxes. Our analyses further demonstrated that the phase-lagged diurnal cycle of SST suppressed deep convection through a decrease in daytime moistening in the lower troposphere. Meanwhile, in the upper ocean, the high-frequency air-sea coupling helped maintain the shallower mixed and isothermal layers by diurnal heating and cooling at the sea surface, which led to a higher mean SST. In contrast, the barely coupled experiments underestimated SST and therefore convective activities. Overall, our results demonstrated that high-frequency air-sea coupling (1 hour or shorter) could improve the reproducibility of the intensity and temporal variation in both diurnal convection and upper ocean processes.

Plain Language Summary

The Madden-Julian Oscillation (MJO) is one of the important sources of atmospheric variability in tropical regions, however, even the modern numerical models could not well reproduce the MJO. We believe that the underestimation of air-sea coupling may cause some parts of such biases in simulating/predicting the MJO. Therefore, our study is aimed to uncover the impact of the air-sea coupling on convection and the related oceanic feature during the MJO. By varying the air-sea coupling frequency, our results showed that the 1-hour or higher frequency coupled experiments had better performance due to the well-reproduced sea surface temperature (SST), while suppressed convection was found in barely coupled experiments. In general, our study suggested that the high-frequency air-sea coupling could improve the reproducibility of both convection and upper ocean features during the MJO.

1 Introduction

The Madden-Julian Oscillation (MJO) is the chief source of variability in tropical regions on the intraseasonal time scale, which features an eastward propagating convectively active envelope (Madden & Julian, 1972). Over the decades, increasing evidence has shown that the MJO not only influences the global climate system but also many types of extreme weather in the tropics and midlatitudes (e.g., Kayano & Kousky, 1999; Kessler, 2001; Lorenz & Hartmann, 2006; Zhang, 2013; Wang & Moon, 2018). Therefore, it is crucial to obtain the successful simulation/prediction of the MJO for tropical weather systems, extreme weather events, monsoons, and the El Nio-Southern Oscillation (Vitart, 2014; Mishra et al., 2017; Wu et al., 2019).

To successfully simulate/forecast the MJO, numerous studies have been carried out; however, some systematic biases remained even in the state-of-the-art climate and forecast models due to the complexities of the MJO (e.g., Madden & Julian, 2005; Peatman et al., 2014; DeMott et al., 2015; Pilon et al., 2016; Kim et al., 2018). Recent studies found that the moistening processes are crucial to the initiation of the MJO and its maintenance/propagation (e.g., Raymond & Fuchs, 2009; Ruppert & Johnson, 2015; Tseng et al., 2015; Nasuno et al., 2015). For example, based on a regional numerical model, Hagos

et al. (2011) demonstrated the important role of the moistening process on stratiform heating and related potential temperature perturbations, and their results also indicated the essence of well-represented shallow- and deep-convection in simulating the MJO. Other studies have mentioned the potential effect of preconditioning moistening on MJO-related rainfall, although the effect may depend on events (e.g., Zermeo-Daz et al., 2015; Chen & Zhang, 2019).

It is now well known that the MJO is a highly air-sea coupled phenomenon from the intraseasonal scale to the subdaily scale (e.g., Waliser et al., 1999; Zhang & Anderson, 2003; DeMott et al., 2015, and the references therein). Numerous studies have demonstrated that the inclusion of air-sea coupling improves the reproducibility of moistening processes during MJO (e.g., Fu et al., 2013; Seo et al., 2014). For example, Kim et al. (2010) suggested that air-sea coupling could improve the intensity and spatiotemporal evolution of the MJO. Seo et al. (2014) further confirmed the improved representation of diurnal sea surface temperature (SST) and the buildup of preconvective warming and moistening in highly coupled models. Based on the *in situ* observations, Ruppert and Johnson (2015) demonstrated that diurnally varying SST could invigorate net column moistening aloft. Some recent studies also suggested that the feedback of SST (hence, air-sea coupling) maintained propagation of the MJO (e.g., Webber et al., 2010; Zhu et al., 2017).

Although the importance of air-sea coupling on convection and the MJO has been well established, few studies have examined detailed modulations on the diurnal scale (e.g., Neale & Slingo, 2003; Crueger et al., 2013; Green et al., 2017). What's more, some studies have also shown that the air-sea coupling frequency may modulate the reproducibility of the diurnal cycle of SST (e.g., Shinoda, 2005; Seo et al., 2014). It is reasonable to expect that the modulated SST may further influence the subdaily moistening processes and the MJO (e.g., Ruppert & Johnson, 2015; Hagos et al., 2016; Katsumata et al., 2018). However, such modulations on the SST by air-sea coupling were neglected in most studies and, therefore, remained unclear.

Thus, the goal of this study is to evaluate the effect of air-sea coupling (and the coupling frequency) on convective activities and related upper oceanic variations, especially on the subdaily scale. As part of the ongoing Year of the Maritime Continent (YMC) project (Yokoi et al., 2017, 2019; Nasuno, 2019; Wu et al., 2019), we focus on one MJO event (November 26th to December 4th, 2017; Figure 1b) captured during the YMC-Sumatra 2017 field campaign. In this period, a large number of land- and ship-based *in situ* observations are available, providing a great opportunity to validate the capability of our numerical experiments.

This paper is organized as follows. Section 2 includes descriptions of the model setup, data source and sensitivity experimental designs. Section 3 includes validation of the model performance with and without cumulus parameterizations. Section 4 documents the impact of coupling frequencies on the convection and surface conditions, along with analyses of the heat and moisture budgets. In Section 5, the role of the daily mean SST and how the SST was modulated by the coupling frequency are discussed. Finally, a summary of the major findings is presented in Section 6. Results on the cumulus parameterizations and extra experiment for the role of local SST are presented in Sections S1 and S2 in the Supporting Information Section.

2 Model and experiment settings

2.1 Model

In this study, numerical experiments were based on the Coupled-Ocean-Atmosphere-Wave-Sediment Transport (COAWST) Modeling System (Warner et al., 2010), and, for simplicity, we excluded the wave and sediment components and only activated the at-

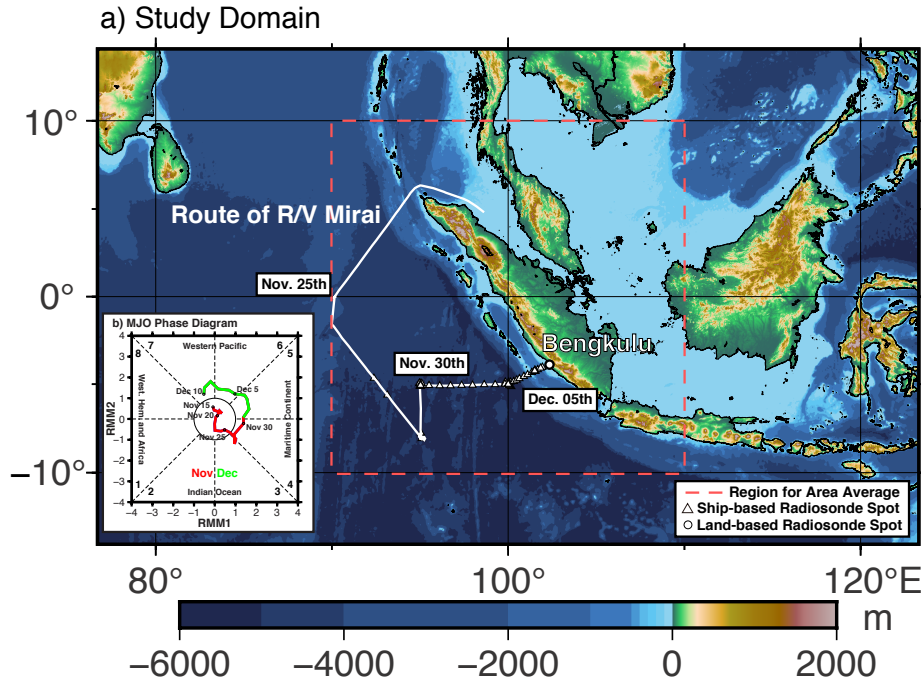


Figure 1. (a) Map of the study domain together with the route of R/V *Mirai* and the locations where the radiosonde was launched. The box enclosed by the red dashed line presents the Sumatra region for area averaging. The inner panel (b) presents the MJO RMM index obtained from the Bureau of Meteorology, Australia.

110 atmospheric (Weather Research and Forecasting Model, WRF V4.1.2) and oceanic (Re-
 111 gional Ocean Modeling System, ROMS svn 980) components. In coupled experiments,
 112 WRF uses the SST calculated by ROMS, while ROMS receives heat fluxes, wind stress,
 113 surface temperature, relative humidity, and freshwater fluxes. In uncoupled experiments,
 114 WRF was activated alone using the satellite-based SST.

115 The model was designed to cover the region from 78°E to 122°E and 14°S to 14°N,
 116 where the center is located at Sumatra Island (0°, 100°E; Figure 1a). All simulations
 117 started at 0:00 UTC on November 21st and ran until 0:00 UTC on December 6th, which
 118 was 5 days prior to the active phase of the MJO over the Maritime Continent (Phase
 119 4 & 5, Figure 1b).

120 The horizontal resolution of WRF and ROMS is 7 km with matching grids and land-
 121 sea masks (Nasuno 2019). The 30 s Global Multiresolution Terrain Elevation Data 2010
 122 (Danielson & Gesch, 2011) and ETOPO1 (Amante & Eakins, 2009) were used for WRF
 123 and ROMS, respectively. WRF has 45 sigma layers from the surface to the top (50-hPa),
 124 and ROMS has 50 layers based on the quadratic Legendre polynomial function (Souza
 125 et al. 2015) with a larger number of vertical levels in the upper 50 m.

126 WRF uses the single-moment 7-class microphysics scheme (Bae et al., 2018), the
 127 Yonsei University PBL scheme (Hong et al., 2006), the Revised MM5 surface layer scheme
 128 (Jimnez et al., 2012), the Unified Noah Land Surface Model (Tewari et al., 2004), the
 129 RRTMG Shortwave and Longwave Schemes (Iacono et al., 2008), and the Grell-Freitas
 130 Ensemble (GFE) cumulus scheme (Grell & Freitas, 2014). ROMS uses the Mellor-Yamada
 131 Level-2.5 closure scheme associated with the third-order upstream horizontal advection,

132 harmonic horizontal mixing, and 4th-order centered vertical advection, and no nudging
133 term is included.

134 It is worth noting that at a so-called gray zone resolution (Gerard, 2007), the cum-
135 ulus parameterization does not always enhance the reproducibility in our 7-km model.
136 Therefore, we conducted extra experiments to obtain the best performance, and results
137 can be found in the Supporting Information Section. The schemes we tested included
138 the GFE scheme (Grell & Freitas, 2014), the New Simplified Arakawa-Schubert (NSAS)
139 scheme (Kwon & Hong, 2017), and the Multiscale KainFritsch (MKF) scheme (Zheng
140 et al., 2016). We also tested the New Tiedtke (NT) scheme (Zhang & Wang, 2017), which
141 is not scale-aware but includes both deep and shallow cumulus components. Note that
142 because the NSAS scheme does not have the shallow convection component, which was
143 proved to be important in simulating convection (Pilon et al., 2016), we applied the Global/Regional
144 Integrated Model system (GRIMs) shallow convection scheme (Hong & Jang, 2018) in
145 CP1HC3 following Kwon and Hong (2017).

146 2.2 Data

147 In this study, the National Centers for Environmental Prediction (NCEP) Final
148 (FNL) Operational Global Analysis data (NCEP, 2000) and Global Ocean Forecasting
149 System (GOFS) 3.1 (Cummings, 2005) were used as the initial and lateral boundary con-
150 ditions for WRF and ROMS, respectively. Additionally, in uncoupled experiments, the
151 daily Optimum Interpolation SST (OISST) dataset was used for the lower boundary con-
152 dition (Banzon et al., 2016; Reynolds et al., 2007). The modeled atmospheric and oceanic
153 properties were saved every 1 hour over the course of each computation in all experiments.

154 For the model validation, we used precipitation data from the satellite-based hourly
155 Global Rainfall Map (GSMaP) dataset together with ship-based [Research Vessel (R/V)
156 *Mirai*] and land-based (Bengkulu, Indonesia) radiosonde data obtained during the YMC-
157 Sumatra 2017 field campaign (Nasuno, 2019; Wu et al., 2019; Yokoi et al., 2019).

158 2.3 Sensitivity experiments of coupling frequency

159 To investigate the influence of the coupling frequency on convection during the MJO
160 active phase, a set of experiments was carried out by varying the coupling interval from
161 30 minutes to 1 day and an uncoupled experiment (WRF-only). ROMS and WRF were
162 coupled at the first-time step of each experiment and then coupled after the specified in-
163 terval. For example, the 6-hourly coupled model would exchange atmospheric and oceanic
164 information at 0:00 UTC, 6:00 UTC, 12:00 UTC, and 18:00 UTC. In addition, Three un-
165 coupled (WRF-only) experiments were further conducted to discuss the role of daily mean
166 SST (see subsection 5a and Section S2). Detailed descriptions of the sensitivity exper-
167 iments can be found in Table 1.

168 3 Model validation

169 Figure 2 shows the horizontal distributions of the mean precipitation rates and max-
170 imum precipitation time during the active phase of the MJO (Nov. 26th-Dec. 4th) ob-
171 tained by satellite and CP1HC. The heaviest rain occurred over the Gulf of Thailand
172 near the eastern coast of the Malay Peninsula and the southern Andaman Sea (Burma
173 Sea), along with a weak but widely distributed rainy zone covering the Indian Ocean and
174 the Maritime Continent (Figure 2a). In the Southern Hemisphere, clear rainy zones were
175 observed over the Indian Ocean, south of the equator and south of Java Island, but the
176 precipitation rates were smaller. All the patterns mentioned above were successfully re-
177 produced in CP1HC, although the rainy regions were not as concentrated as the obser-
178 vations in the Southern Hemisphere.

Table 1. Descriptions of sensitivity experiments

Experiment	Settings
CP30MC	30-min WRF-ROMS
CP1HC	1-h WRF-ROMS
CP3HC	3-h WRF-ROMS
CP6HC	6-h WRF-ROMS
CP12HC	12-h WRF-ROMS
CP1DC	1-d WRF-ROMS
NOCP	WRF-only (OISST)
NOCP+	WRF-only (OISST & daily mean SST from CP1HC)
NOCP++	WRF-only (daily mean SST from CP1HC)

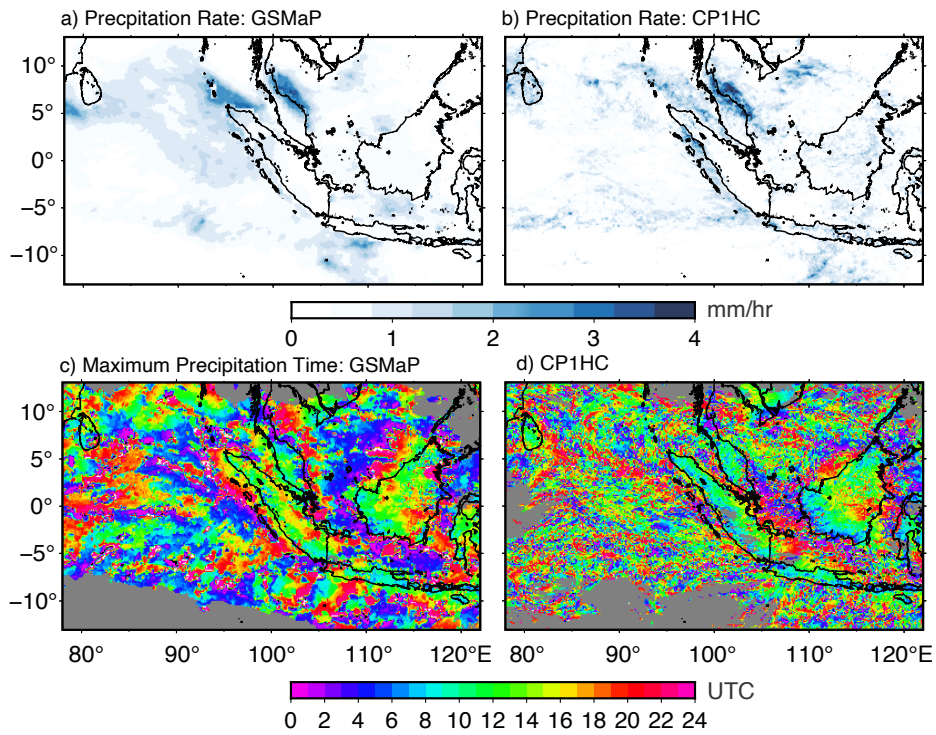


Figure 2. Horizontal distributions of precipitation rates and the time of maximum precipitation obtained from satellite observations (a and c) and CP1HC (b and d).

179 In addition to the precipitation rate, the time of maximum precipitation can also
 180 be regarded as an important indicator representing the diurnal cycle of precipitation. As
 181 shown in Figure 2c, the maximum precipitation mainly occurred in the evening near the
 182 coastal region and in the early morning inland (see the patterns over Sumatra and Kali-
 183 mantan). Meanwhile, over the shallow coastal seas, the heaviest rain occurred in the early
 184 morning, especially near the Gulf of Thailand and west of Sumatra Island where the heav-
 185 iest rainfall was observed. In general, the observed diurnal cycle he observed diurnal cy-
 186 cle was consistent with the diurnal cycle revealed in previous studies (Neale & Slingo,
 187 2003; Mori et al., 2004). Moreover, in comparison with the observations, the precipita-
 188 tion in CP1HC reached its maximum rate at the same time (Figure 2d), although the
 189 simulated precipitation showed more small-scale features.

190 In addition, we further compared our model results with the *in situ* radiosonde pro-
 191 files obtained during the YMC-Sumatra 2017 field campaign (Figure 3; also see Figure
 192 1a for the locations of radiosonde observations). The atmosphere near Sumatra Island
 193 was dominated by the westerly wind over the entire active phase of the MJO, which could
 194 also be seen in the model. The meridional wind component (v) suggested that a tran-
 195 sition of wind field occurred after Nov. 30th, as shown by the opposite meridional wind
 196 direction before and after the day. A similar transition of the meridional wind could also
 197 be found in our model, but with some underestimations. Moreover, both observations
 198 and simulations showed that very high relative humidity (RH) was dominant from the
 199 surface to the upper troposphere, indicating the vigorous convective activities occurred
 200 in both the model and real atmosphere.

201 Overall, our model showed good agreement with both satellite-based and *in situ*
 202 observations, suggesting that our model is reliable; therefore, we conducted sensitivity
 203 experiments of coupling frequencies using the same schemes and settings as CP1HC.

204 4 Results

205 4.1 The impact on the atmospheres

206 To examine the impact of the air-sea coupling frequency on convection, we first fo-
 207 cused on the moisture and moisture fluxes in our sensitivity experiments. Figure 4a presents
 208 the map of the daily mean precipitable water (PW) and vertically integrated moisture
 209 fluxes averaged during the active phase of the MJO (from surface to 300-hPa, Novem-
 210 ber 26th to December 4th) in CP1HC. A large amount of PW was concentrated north
 211 of Sumatra Island and the Malay Peninsula, which consists of the location of the heav-
 212 iest rainfall, as observed by satellite and CP1HC (Figure 2). The cyclonic gyre located
 213 in both north and south of the equator, associated with the jet-like moisture fluxes orig-
 214 inating from the Indian Ocean to the west (also from the South China Sea), exhibited
 215 the existence of vigorous convective activities over the Maritime Continent (i.e., the ac-
 216 tive phase of the MJO).

217 In comparison with CP1HC, the differences in the mean PW and moisture fluxes
 218 were not obviously changed in CP30MC, CP3HC, or CP6HC. However, unlike the highly
 219 coupled experiments (i.e., 6 hours or more coupled), the total amount of PW decreased
 220 by 5 mm or more in most regions in the barely coupled models, with the clearest pat-
 221 tern in the uncoupled experiment (NOCP, Figure 4g). Meanwhile, the moisture flux
 222 anomalies showed anticyclonic gyre-like and westward jet-like patterns, indicating greatly
 223 suppressed convective activities (Figure 4e-g). Note that although the anticyclonic gyre-
 224 like pattern could also be seen in Figure 4d, no westward anomalies were found, suggest-
 225 ing that the convection was weakened in the CP6HC but not as much as that in the barely
 226 coupled/uncoupled experiments.

227 Figure 5a presents the frequency-altitude distributions of RH over the seas near
 228 Sumatra Island (red box in Figure 1a; Nasuno et al. 2015). The lower troposphere (sur-

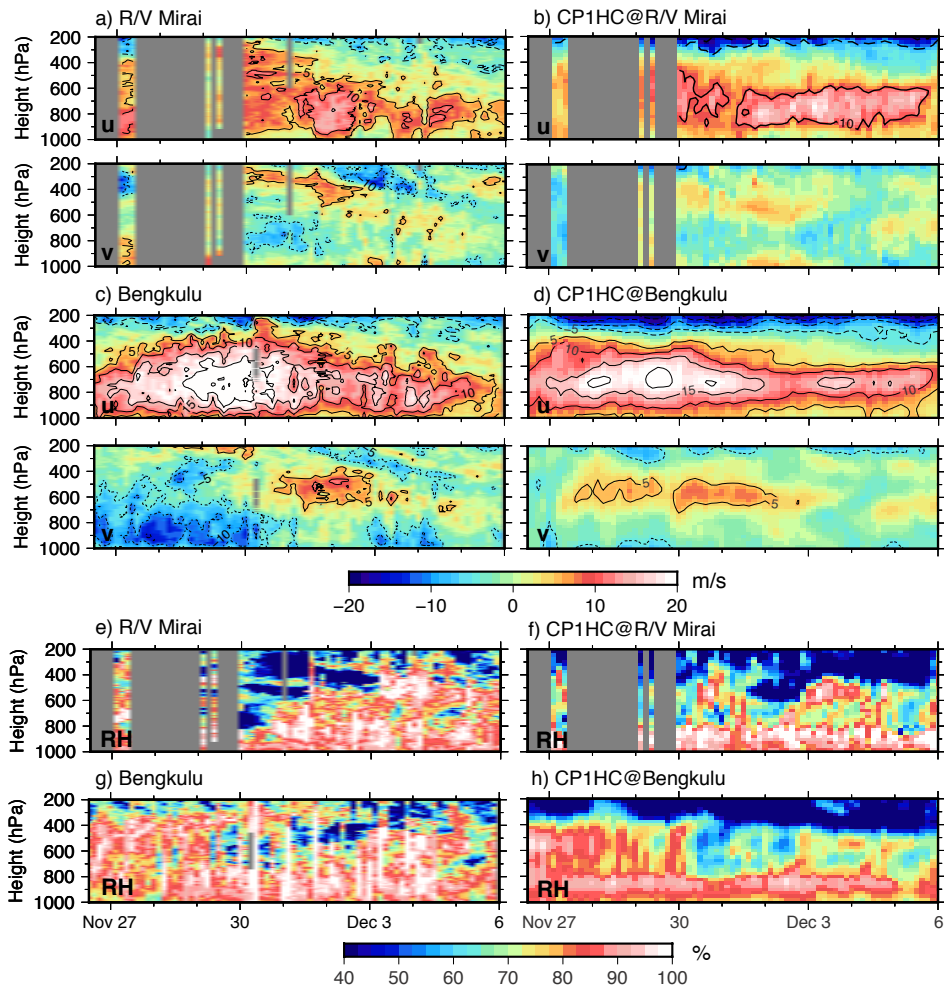


Figure 3. Vertical profiles of wind and relative humidity obtained by CP1HC and radiosonde observations obtained during the YMC-Sumatra 2017 field campaign.

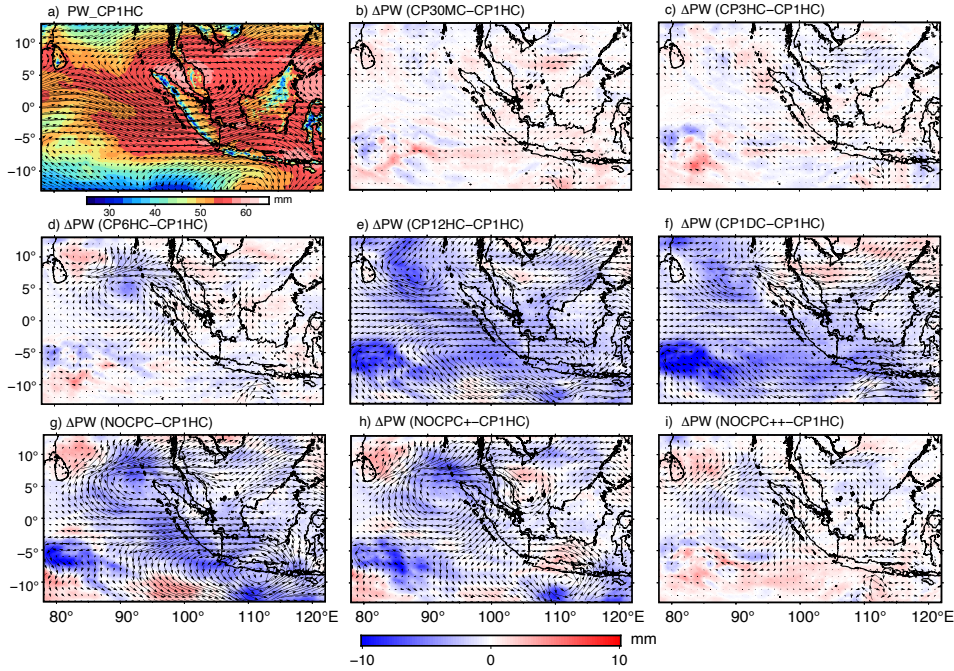


Figure 4. Horizontal distributions of the precipitable water and moisture fluxes integrated from the surface to 300-hPa height during the active phase of the MJO (November 26th to December 4th) in (a) CP1HC and (b-h) the differences between CP1HC and other runs.

229 face to 800-hPa level) was characterized by frequent occurrences of 80-100% RH. The
 230 frequency in the middle troposphere (850-500 hPa) ranged from 50% to 100% RH, where
 231 70-80% RH occurred the most. Above the 500-hPa level, the atmosphere became increas-
 232 ingly drier as the height increased. The other highly coupled experiments showed only
 233 small differences (Figure 5b-d) from CH1HC. In the 30-minute coupled experiment, the
 234 increased (decreased) frequency of $> 70\%$ RH ($< 70\%$ RH) suggested that the convective
 235 activities were more enhanced. However, this was not the case in the barely coupled/uncoupled
 236 experiments. The occurrences of $> 70\%$ RH (hereafter, high RH) were greatly reduced
 237 from the lower troposphere to the upper levels, and $> 90\%$ RH was nearly extinct in the
 238 midlevels (Figure 5e-g). Accordingly, low RH appeared more frequently in nearly the entire
 239 column above the atmospheric boundary layer in the barely coupled/uncoupled exper-
 240 iments, suggesting that convection was greatly weakened.

241 One may consider that the reduction in high RH may be caused by the modulated
 242 preconditioning of the MJO (e.g., Seo et al. 2014). However, our models showed differ-
 243 ent results. As shown in Figure 6, the occurrences of high RH ($> 70\%$) showed no sig-
 244 nificant differences before the MJO, even at in midlevels (Figure 6c). Nevertheless, the
 245 situation started to change only after the MJO entered phase 4 (November 26th-30th,
 246 Figure 1b), although the SSTs had already been modulated since the model initiation
 247 (see Figure S3 in the Supporting Information). In particular, the atmosphere was greatly
 248 moistened in the highly coupled experiments ($> 90\%$ occurrence of high RH), which con-
 249 sisted of the vigorous convection during the MJO. Nonetheless, the barely coupled/uncoupled
 250 experiments showed relatively lower values, as suggested by the clear separation in the
 251 middle troposphere among the experiments. The occurrence of high RH in the barely
 252 coupled/uncoupled experiments was approximately 10% lower than that in the highly
 253 coupled experiments. As the MJO propagated to the east (after December 1st, i.e., phase
 254 5 of the MJO), convection was suppressed in all experiments (see the descending trend

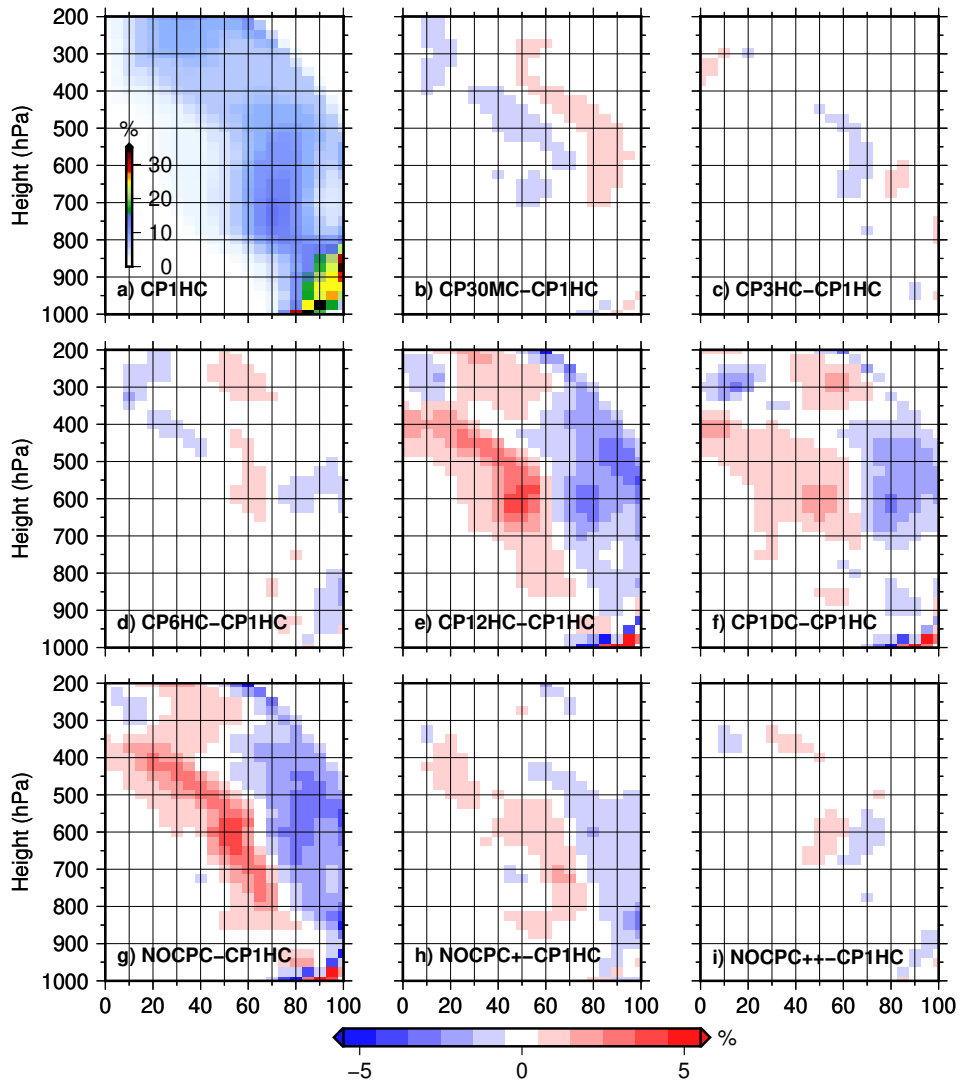


Figure 5. The frequency-altitude distributions of the simulated relative humidity over the seas around Sumatra Island (10°S - 10°N , 90° - 110°E ; red box in Figure 1a).

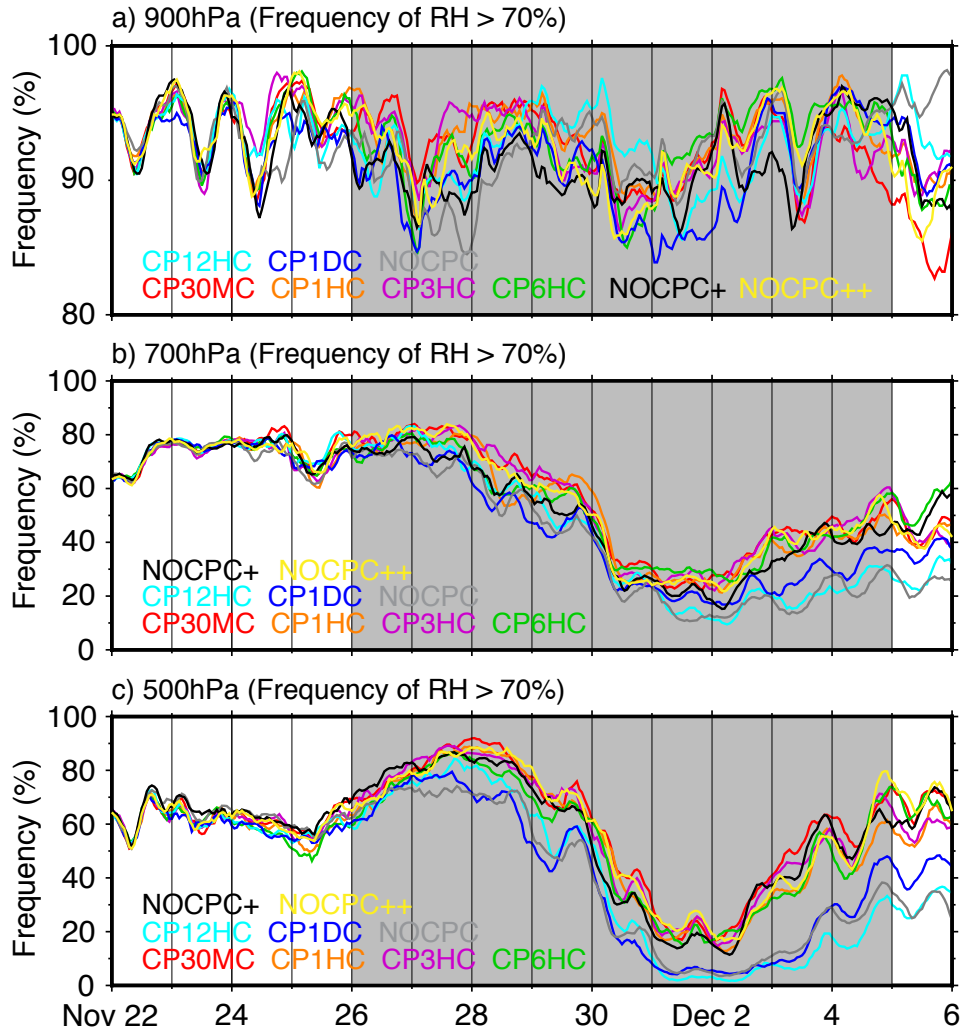


Figure 6. Time series of frequencies (occurrences) of the grid with high relative humidity (> 70%) at the (a) 900-hPa level, (b) 700-hPa level, (c) 500-hPa level, and time series of (d) vertical accumulated divergence of moisture fluxes from the surface to the 800-hPa level.

255 in Figure 6), but the differences became larger. Overall, our results suggested that the
 256 high-frequency air-sea coupling enhanced the convective activities during the active phase
 257 of the MJO, and it also helped with the maintenance of the moist atmosphere after the
 258 MJO passed.

259 4.2 Modulated diurnal cycle at the sea surface

260 Figure 7 represents the diurnal composite of surface variables averaged in the Sumatra
 261 region (red box in Figure 1a and ocean only). The SSTs reached over 29.5 °C in the
 262 highly coupled experiments, along with a clear diurnal cycle that was absent in the barely
 263 coupled/uncoupled experiments. Although the daily mean SST and its diurnal ampli-
 264 tude were nearly identical among the highly coupled experiments (Table 2), the tempo-
 265 ral variations were not. In CP1HC and CP30MC, the largest SST appeared at 8:00 UTC,
 266 which consisted of a recent study based on buoy data (Morak-Bozzo et al., 2016). How-
 267 ever, this was not the case in CP3HC (CP6HC), where the diurnal cycle of SST was de-

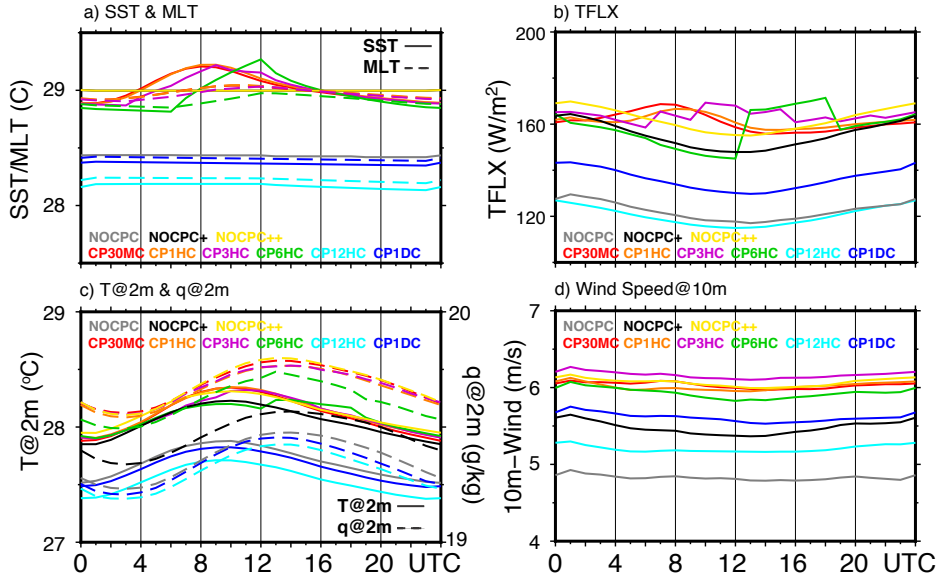


Figure 7. Diurnal composites of (a) sea surface temperature (solid line) and mixed-layer temperature (dashed line), (b) turbulent heat fluxes (the sum of surface sensible and latent heat fluxes, upward positive), (c) surface air temperature (solid line) and specific humidity (dashed line) at 2 m, and (d) surface wind speed at 10 m. Colors represent different experiments. Note that the correspondence of color and experiment is consistent in this paper, except Figure 14.

268 layed by 1 hour (4 hours). On the other hand, CP12HC and CP1DC did not have any
 269 diurnal cycle of SST, and the mean values were also lower than those of highly coupled
 270 experiments.

271 The surface turbulent heat fluxes (TFLX; upward positive), which are mainly controlled
 272 by the latent heat flux (see Figure S5 in the Supporting Information), had more
 273 complex variations. The TFLX in CP30MC started increasing at 16:00 UTC and finally
 274 reached its maximum at 7:00 UTC (14:00 LT in the Sumatra region), followed by a 9-
 275 hour decrease. Similar variations could be found in CP1HC, although its largest TFLX
 276 appeared 1 hour later and smaller. The lag became larger in CP3HC, along with a 2-
 277 hour period fluctuation caused by the different response times of surface air tempera-
 278 ture (T2m) and specific humidity (q2m) (Figure 7c; also see Figure 13d for the lead-lag
 279 correlation).

280 Among the highly coupled experiments, CP6HC showed totally different trends:
 281 the TFLX monotonically decreased during the daytime and then suddenly increased after
 282 12:00 UTC. Such unrealistic variations were generated by the coupling procedure used
 283 in our model. Except for the time step of coupling, both WRF and ROMS used a con-
 284 stant boundary forcing at most of the time steps. For example, in the CP6HC, the in-
 285 creasing SST from 6:00 UTC to 12:00 UTC only occurred in the ocean (ROMS), while
 286 WRF used the temporally constant SST (which was obtained at 6:00 UTC) until the next
 287 coupling time. Therefore, the underestimation and overestimation occurred continuously
 288 due to the constant forcing.

289 Unlike the SST and TFLX, the surface air temperature (T2m) and specific humid-
 290 ity experienced the same diurnal cycle in all experiments, although they were 0.5 °C and
 291 0.25 g/kg higher in the highly coupled experiments (Figure 7c). Despite the unique vari-

Table 2. Daily Mean SST and TFLX in the Sumatra Region

Experiment	SST (°C)	TFLX (W/m ²)
CP30MC	29.02	161.04
CP1HC	29.02	161.30
CP3HC	29.01	163.85
CP6HC	28.96	158.55
CP12HC	28.17	120.02
CP1DC	28.36	135.95
NOCPC	28.43	122.22
NOCPC+	29.00	155.03
NOCPC++	29.00	161.87

292 ations in CP6HC, the heating of surface air started at 1:00 UTC, leading to the high-
 293 est T2m at 9:00 UTC. The increase in q2m started slightly later at 3:00 UTC and then
 294 reached its maximum at 13:00 UTC (Figure 7c).

295 The surface wind speed had nearly no diurnal cycle regardless of coupling frequen-
 296 cies, but it was 1 m/s higher in the highly coupled experiments (Figure 7d). Note that
 297 the bimodal variations in T2m and its earlier increase than the SST in the CP6HC were
 298 mainly caused by phase-delayed heating from the ocean after 12:00 UTC, which allevi-
 299 ated the nighttime temperature decrease.

300 Without the diurnally varying surface forcing, the SSTs were nearly constant in
 301 the barely coupled experiments. Unlike the increasing trends during the daytime in the
 302 highly coupled experiments, their TFLXs decreased during the daytime and increased
 303 during the nighttime, following T2m and q2m with an opposite sign (Figure 7c). Such
 304 variations were similar to the uncoupled experiment (NOCPC). Note that the higher SST
 305 and TFLX in CP1DC were caused by the nonzero solar radiation throughout the day,
 306 while the heating was updated to zero in CP12HC after 12:00 UTC (Figure 13c). More-
 307 over, the influence of the mean SSTs and its diurnal cycle can be found in Section 5.

308 4.3 Heat and moisture budget analysis

309 To further elucidate the influence of the coupling frequency on subdaily moisten-
 310 ing processes, we executed an area-averaged heat and moisture budget analysis. We re-
 311 arranged the budget equations including the apparent heat source (Q1) and moisture
 312 sink (Q2) following Yanai et al. (1973):

$$\frac{\partial s}{\partial t} \equiv Q_1 - \vec{U} \cdot \nabla s - \omega \frac{\partial s}{\partial p}, \quad (1)$$

$$L_v \frac{\partial q}{\partial t} \equiv -Q_2 - L_v \vec{U} \cdot \nabla q - L_v \omega \frac{\partial q}{\partial p}, \quad (2)$$

313 where $s \equiv c_p T + gz$ is the dry static energy, c_p is the specific heat at constant pres-
 314 sure, T is the temperature, q is the specific humidity, L_v is the latent heat of conden-
 315 sation, and \vec{U} and ω are the horizontal wind vector and the vertical wind component in
 316 pressure coordinates, respectively. All terms were calculated based on the hourly out-
 317 put from the model and averaged over the Sumatra region (ocean only, red box in Fig-
 318 ure 1a) during the MJO active phase.

319 Figure 8 represents the diurnal composite time-altitude distributions of the s and
 320 q budgets averaged in the Sumatra region during the MJO active phase based on CP1HC.
 321 The atmosphere became warmer during the local daytime and cooler during the local

322 nighttime, shifting its phase at 12:00 UTC (Figure 8a). On the other hand, diurnal moist-
 323 ening mainly occurred from 4:00 UTC (11:00 LT) at surface levels, and such moisten-
 324 ing generally takes 4-5 hours to extend to the entire lower levels (Figure 8b). Although
 325 the positive Q1 could be seen all day long during the MJO, the strong heating started
 326 at 16:00 UTC (23:00 LT) in the middle troposphere and reached its maximum at 4:00
 327 UTC (Figure 8c), while the corresponding moisture sink occurred slightly earlier at lower
 328 levels before the heating started (Figure 8d). Both Q1 and Q2 were basically balanced
 329 by vertical advection (s_{adv} and q_{adv} , Figure 8g and 9h, respectively), indicating the
 330 existence of vigorous convection, while horizontal moisture advection (q_{hadv} ; Figure 8f)
 331 tended to dry the atmosphere due to the background eastward moisture fluxes during
 332 the MJO (Figure 4a). Note that, in this study, we only focused on the air-sea interac-
 333 tion and convection above the ocean, so that the time evolutions of Q1 and Q2 may in-
 334 clude some influences from the diurnal land-sea circulation; however, such influences were
 335 neglected during the analyses.

336 Although the differences between CP6HC and CP1HC were small in the PW and
 337 high RH occurrences (Figures 4 and 5), the budget analyses showed more detailed mod-
 338 ulations. It is easy to find that the heating (moistening) was stronger (weaker) during
 339 the nighttime (daytime) in the CP6HC (Figures 9a and 9b), which was likely due to the
 340 phase-lagged SST and related TFLX. In addition to the phase lag in the diurnal pro-
 341 cesses, both Q1 and Q2 were weakened, associated with the reduced vertical advection
 342 of moisture. It is suggested that the phase-delayed diurnal cycle of SST greatly weak-
 343 ened the daytime convection and slightly enhanced the nighttime convection, resulting
 344 in a net reduction in daily mean state. Note that the shifted diurnal variations in heat/moisture
 345 in the CP6HC not only influenced the convection over the ocean but also overland, in-
 346 ducing an unrealistic diurnal cycle of precipitation (figures not shown).

347 In the uncoupled run, Q1 and Q2 were significantly reduced over 0.1 K/hr, asso-
 348 ciated with the weakening in vertical advection (Figure 10). Whats more, the positive
 349 anomalies in horizontal moisture advection (q_{adv}) also indicated that the eastward mois-
 350 ture transport was reduced, which consisted of the easterly moisture flux anomalies, as
 351 shown in Figure 4g. As a result, the atmosphere became warmer (cooler) and drier (moister)
 352 during the daytime (nighttime) in NOCPC (Figure 10c and 10d). In general, the results
 353 shown above suggested that the convection and diurnal heat/moisture processes were
 354 greatly modulated when using the daily mean SST; however, to investigate the roles of
 355 the mean SST and its diurnal cycle, further experiments were needed (see the discus-
 356 sion section).

357 5 Discussion

358 5.1 The role of the daily mean SST

359 In our model, WRF-only received the SST from ROMS. The SSTs in CP12HC, CP1DC,
 360 and NOCPC were >0.6 °C lower than those in the highly coupled experiments, which
 361 may therefore be the key factor in the weakened convective activities (e.g., Dipankar et
 362 al., 2019). To confirm this, two extra WRF-only experiments were carried out by using
 363 the same settings in NOCPC but with modified SSTs. In NOCPC+, we replaced the OISST
 364 with the daily mean SST obtained from CP1HC within the Sumatra region (red box in
 365 Figure 1a), and such replacement was applied everywhere in the model domain in NOCPC+.
 366 One may notice that the SST in NOCPC+/NOCPC++ was slightly lower than that in
 367 CP1HC, which induced the linear interpolation of the daily mean SST into the 6-hourly
 368 SST, following the same procedure for the OISST in NOCPC. Fortunately, our results
 369 show that the biases were small and negligible (~ 0.02 °C, Table 2). Note that we only
 370 discussed the role of daily mean SST based on NOCPC++, and readers may refer to Sec-
 371 tion S2 in the Supporting Information for more results of the local SSTs.

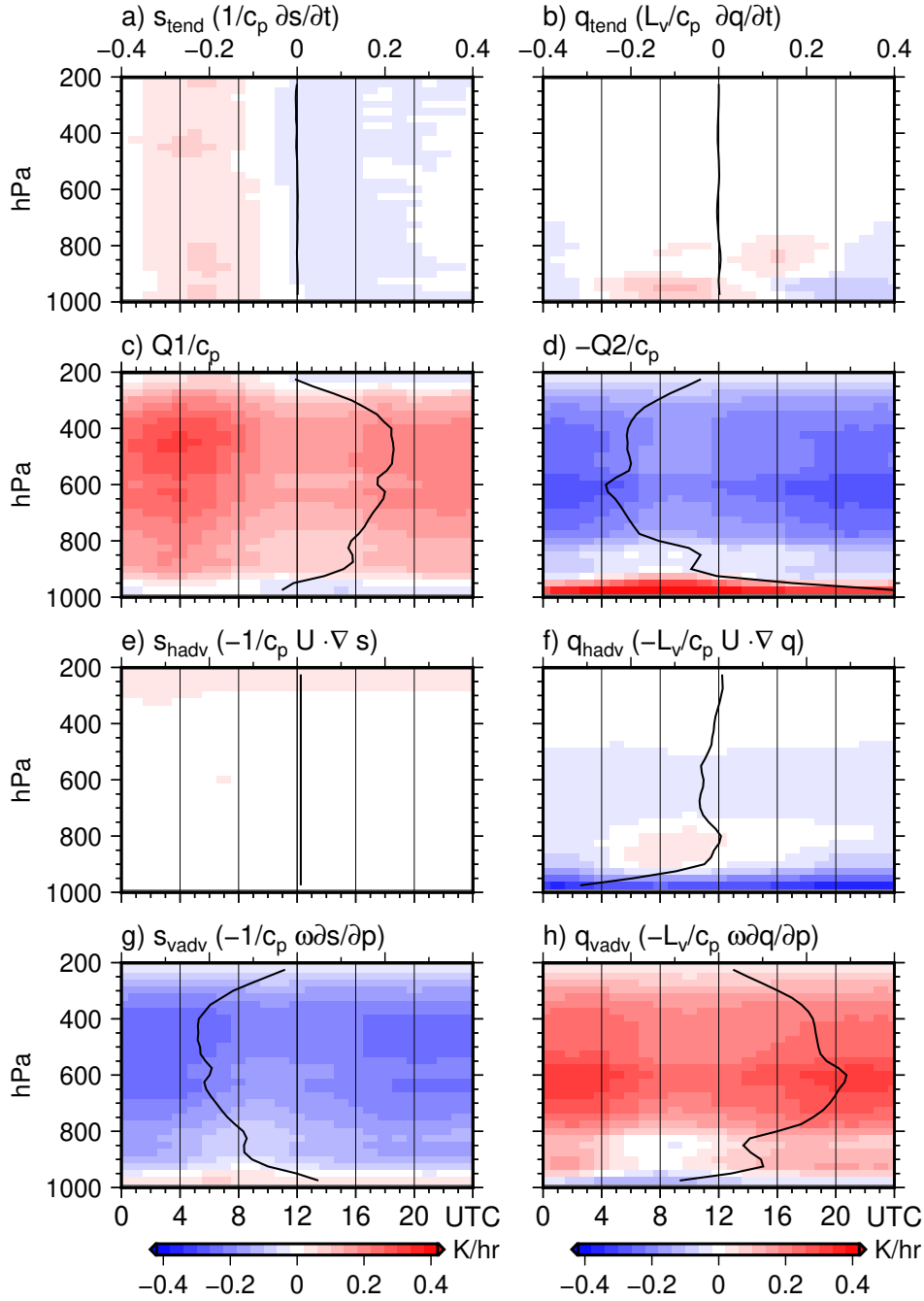


Figure 8. Diurnal composites of (a) tendency term, (c) apparent heat source $Q1$, (e) horizontal advection term, and (g) vertical advection term. Panels (b), (d), (f) and (h) are the same but for the moisture budget. The vertical distribution of daily mean values is also shown in each panel.

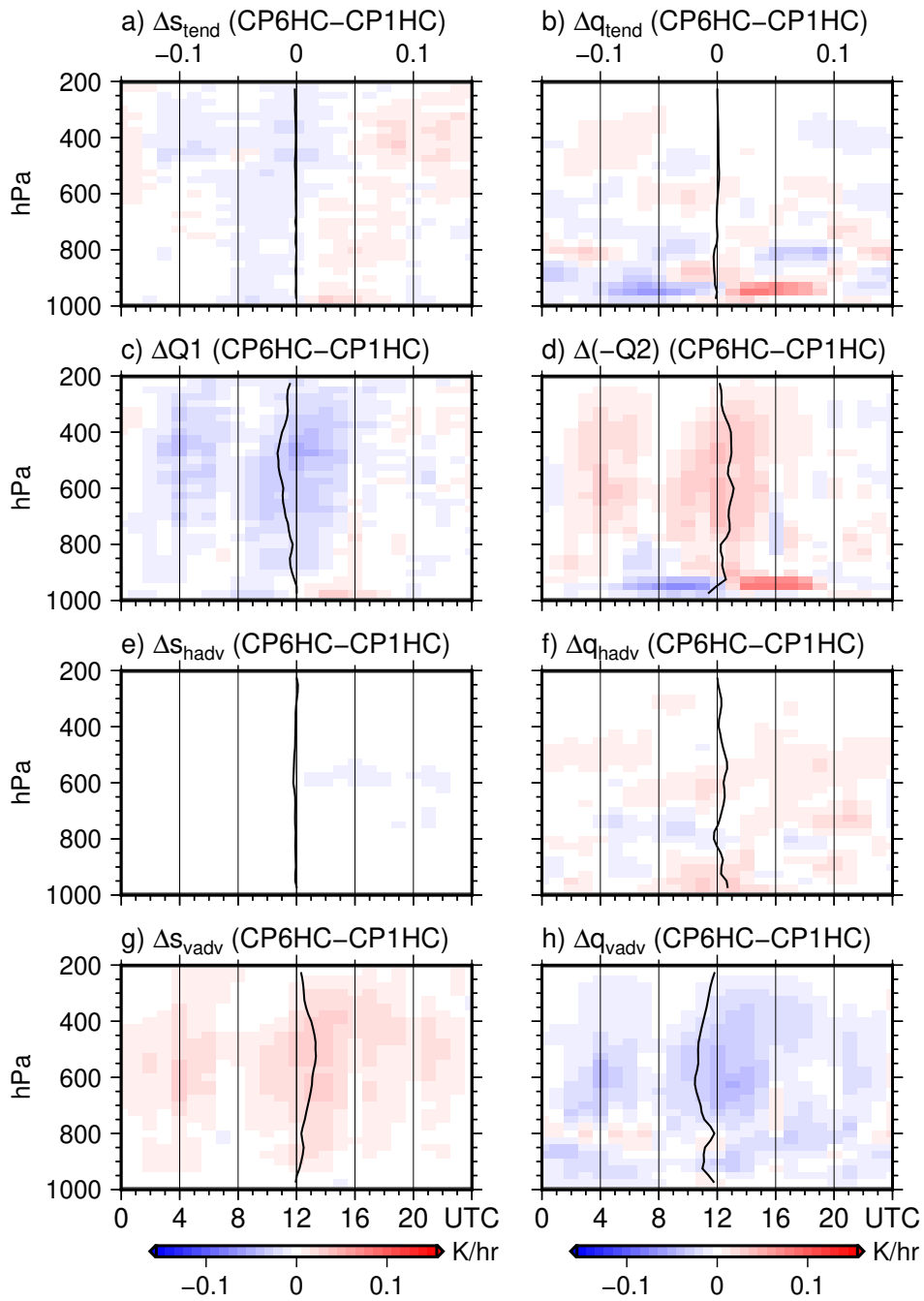


Figure 9. Same as in Figure 8 but for the differences between CP6HC and CP1HC.

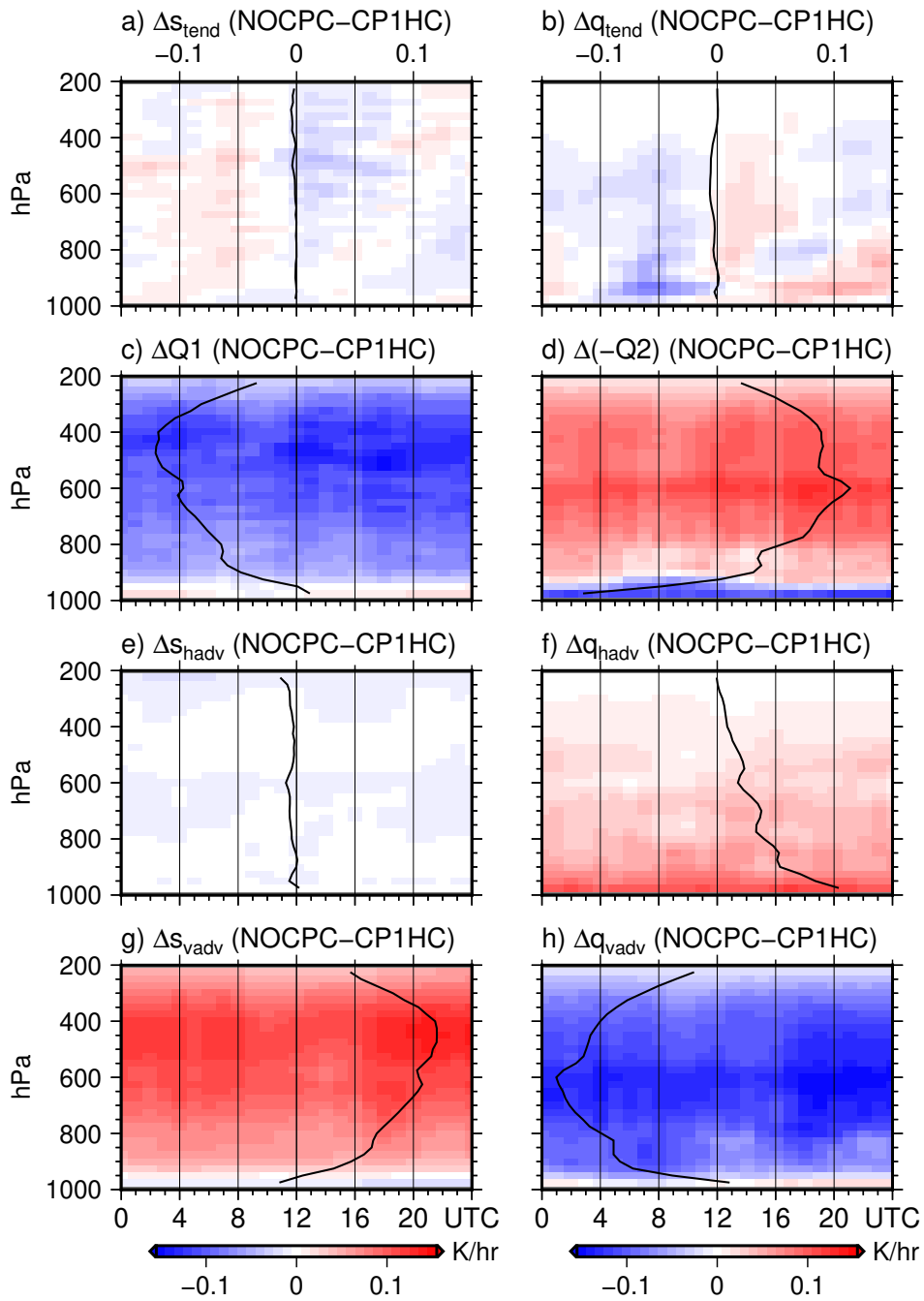


Figure 10. Same as in Figure 8 but for the differences between NOCPC and CP1HC.

372 In general, the higher SST induced the higher TFLX (Table 2 and Figure 7), more
 373 active convection (Figure 6), and therefore a moister atmosphere (Figure 4), which was
 374 almost comparable with those in highly coupled experiments. Whats more, with the same
 375 daily varying SST, the time evolution of convective activities also showed good agree-
 376 ments with the highly coupled models during the MJO. The anticyclonic gyre-like pat-
 377 tern of moisture flux anomalies remained, along with the small but negative biases in
 378 PW, although its center moved to the south. It is suggested that the underestimation
 379 of convection remained in NOCPC++, even with the same daily mean SST.

380 As showed in Figure 11, both Q1 and Q2 had small but nonnegligible negative anoma-
 381 lies from the surface to the midlevels. Moreover, unlike the monotonic reductions in NOCPC,
 382 the differences in NOCPC++ showed more subdaily variations. We found that the lower
 383 (higher) SST induced a drier (moister) boundary layer in NOCPC++ during the day-
 384 time (nighttime). Previous studies suggested that the premoistening of the lower tro-
 385 posphere is an important feature that can promote deep convection (Shinoda & Uyeda,
 386 2002; Katsumata et al., 2018). Therefore, it is likely that this weakened moistening in
 387 the lower levels of NOCPC++ (approximately 5:00-12:00 UTC, Figure 11b) suppressed
 388 the onset of the subsequent diurnal deep convection, resulting in the negative Q1/Q2 and
 389 related vertical advection.

390 Based on the results of CP6HC and NOCPC++, the daily mean SST did play a
 391 dominant role in controlling the convection intensity, while the higher daytime SST (hence,
 392 the diurnal cycle of SST) played a smaller but nonnegligible role in daytime moistening
 393 and therefore the onset of diurnal deep convection. Figure 12 further demonstrates the
 394 above conclusion that while the higher daily mean SST induced larger moisture conver-
 395 gence, small but clear negative biases could be seen after 8:00 UTC in NOCPC++ and
 396 CP6HC, exhibiting weakened diurnal convection.

397 5.2 Modulations in the upper ocean

398 Since we found that the diurnal cycle of SST played a smaller role than the higher
 399 SST, one may ask why the highly coupled experiments had higher SSTs. To answer this
 400 question, we focused on the modulations in the ocean by air-sea coupling, especially the
 401 dynamics of the oceanic mixed layer and upper isothermal layer.

402 In this study, we defined the oceanic mixed-layer depth (MLD) in terms of a depth
 403 with a density equal to that at the 1 m depth plus an increment in density equivalent
 404 to -0.2 °C (Moteki et al., 2018), and therefore, the isotherm depth (ILD) is defined as
 405 the depth where the temperature is 0.2 °C lower than that at 1 m depth. Note that the
 406 results were not significantly changed when the reference depth was set to 10 m.

407 As shown in Figure 7c, the mixed-layer temperature (MLT, vertically averaged within
 408 the mixed layer) in the highly coupled experiments was approximately 29.0 °C, which
 409 was 0.8 °C (0.6 °C) higher than that in CP12HC (CP1DC). Both MLT and MLD had
 410 a weak but clear diurnal cycle, indicating the existence of stratification and destratifi-
 411 cation induced by the surface heating/cooling and mixing processes. The mixed layer
 412 became warmer and shallower after the sea surface was heated during the daytime (Fig-
 413 ure 13a), and the largest MLT appeared 2 to 3 hours after the SST reached its maximum
 414 (Figure 7a), which was the time required by the adjustment processes (Figure 13d). Sim-
 415 ilar diurnal variations were found in ILDs, although it was generally over 10 m deeper
 416 than the MLD in all coupled experiments (Figures 13a).

417 Our results suggested that the mixed layer dynamics could be greatly modulated
 418 with or without high-frequency air-sea coupling. In barely coupled experiments, the MLTs
 419 were relatively higher than the SSTs (Figure 7a) because the ocean experienced net heat
 420 loss at the sea surface throughout the day (Figure 13c and Table 3). It is reasonable to
 421 consider that continuous surface cooling reduced the SST and broke down the upper layer

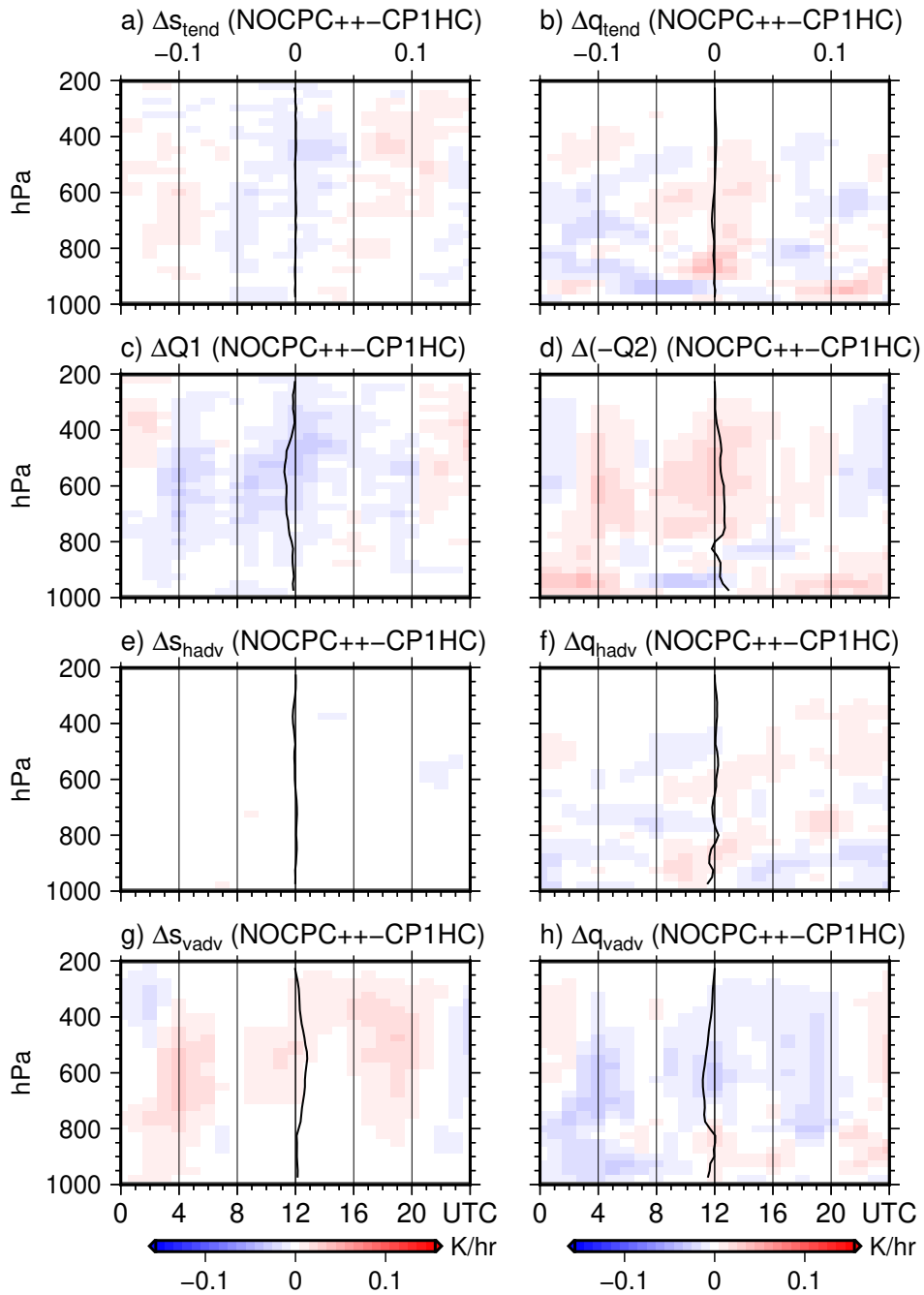


Figure 11. Same as in Figure 8 but for the differences between NOCPC++ and CP1HC.

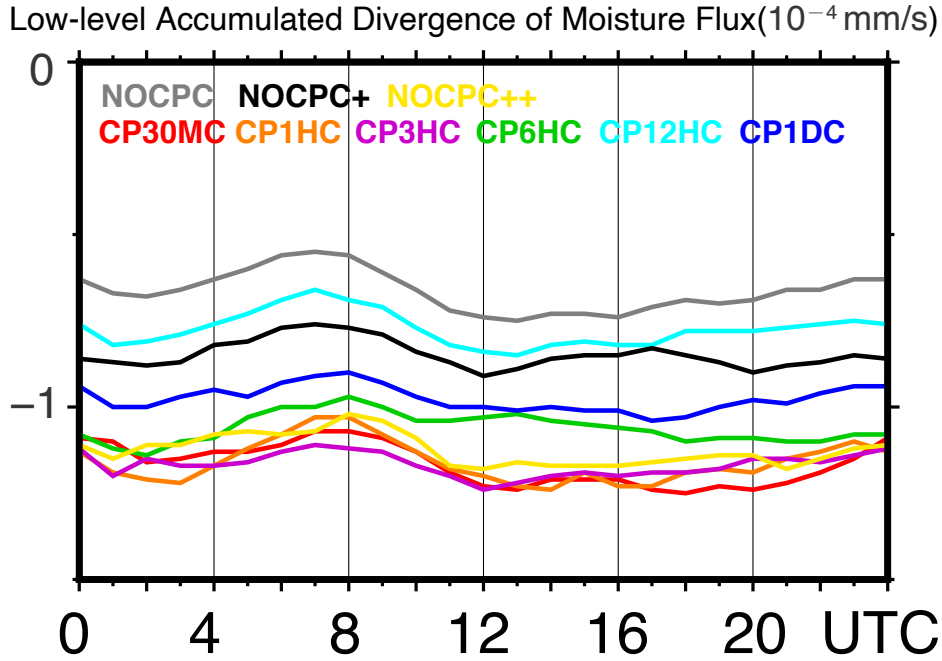


Figure 12. Diurnal composites of frequencies (occurrences) of the high RH (> 70%) around the Sumatra region (90°-110°E, 10°S-10°N; red box in Figure 1) at the (a) 700-hPa level; and (b) 500-hPa level.

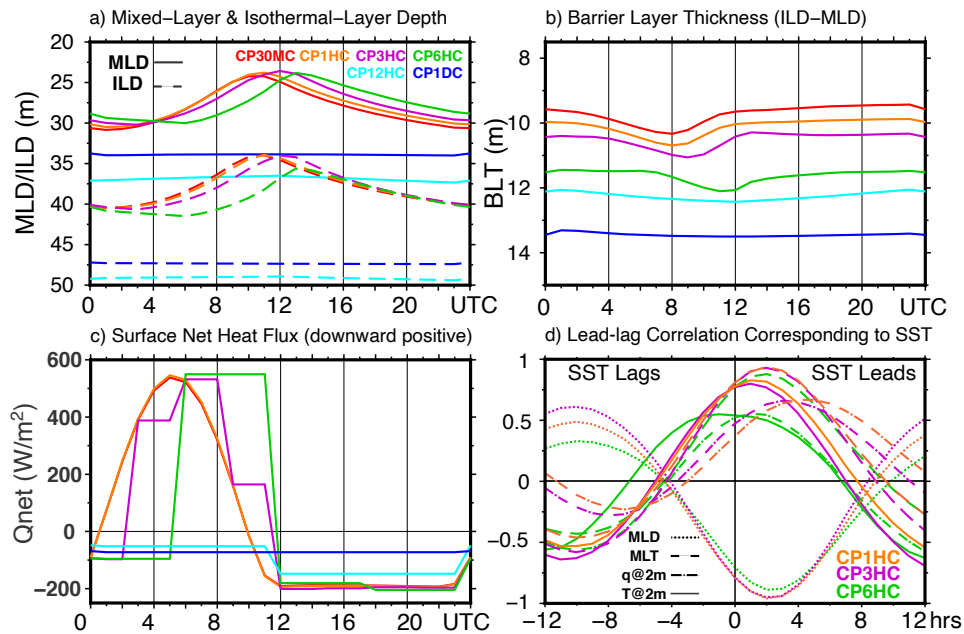


Figure 13. Diurnal composites of (a) the mixed-layer (solid line) and isothermal-layer depth (dashed line), (b) thicknesses of the barrier layer, and (c) the net heat flux at the sea surface (downward positive). (d) The lead-lag correlations of mixed-layer depth (dotted line), mixed-layer temperature (dashed line), surface air temperature (solid line), and specific humidity (dash-dotted line) corresponding to the SST.

Table 3. Daily Mean of Properties in ROMS

Experiment	MLT ($^{\circ}\text{C}$)	MLD (m)	ILD (m)	BL (m)	Net Heat Flux at Sea Surface (W/m^2)
CP30MC	28.98	28.17	37.89	9.72	27.27
CP1HC	28.98	27.78	37.89	1011	28.15
CP3HC	28.97	27.54	38.05	10.51	24.65
CP6HC	28.91	27.56	39.18	11.62	17.54
CP12HC	28.23	36.86	49.11	12.25	-99.64
CP1DC	28.41	33.90	47.35	13.45	-72.49

instability, inducing strong vertical mixing and therefore the deepening of MLD/ILDs. Whats more, the deeper MLD further reduced the MLT. On the other hand, in highly coupled experiments, the net heat gain during the daytime would raise the SST and enhance the stratification that suppresses the mixing, leading to a shallower MLD/ILD. It is easy to find that the high-frequency air-sea coupling helped to maintain the higher SSTs/MLTs and shallower MLDs/ILDs.

Note that although all highly coupled experiments had similar mixed-layer processes (Figure 15d), the MLD (ILD) became relatively deeper (shallower) when the coupling frequency was higher (Table 3), inducing a thinner barrier layer (Figure 13b).

5.3 The drift of SST

Although the higher mean SST was generated by diurnal surface heating/cooling in highly coupled experiments, the SSTs may still be overestimated because of the positive biases from the OISST (satellite-based). On the other hand, as mentioned in previous studies, the OISST generally underestimates the true SST due to spatial smoothing and the removal of diurnal variations (Reynolds et al., 2007; Clayson & Bogdanoff, 2013). Therefore, it is necessary to compare them with the *in situ* observations. In this study, we used the SST measured by the *Mirai* Surface Meteorological observation (SMet) system at 5-m depth (SBE38, SeaBird Electronics). Details of the ship-based observations can be found in the MIRAI MR17-08 Cruise report (JAMSTEC & BPPT, 2018).

Figure 14 shows the time series of SSTs obtained in our models, satellite, and R/V *Mirai* during the active phase of the MJO, together with the precipitation rate observed by the optical rain gauge (ORG-815DR, Osi). The OISST (NOCP) showed negative biases most times, while the models overestimated in some periods. The overestimation of SST on November 28th was mainly related to heavy rainfall, while the period from December 3rd was related to the underestimation of convection and its related precipitation (hence, surface cooling) as showed in Figures 3e and 3f. Nevertheless, both OISST and our modeled SSTs generally followed the trend of *in situ* observations in the same order. In addition, despite the slight underestimation of convection, our model showed good agreement with both satellite-based and *in situ* observations over the entire domain. Therefore, our conclusions on the importance of high-frequency air-sea coupling (and the higher and diurnally varying SST generated by that) are robust and reliable.

6 Concluding Remarks

A regional cloud-resolving coupled model was conducted to evaluate the impact of coupling frequency on convective activities during an MJO event captured in the YMC-Sumatra 2017 field campaign. By activating the scale-aware GFE cumulus scheme, the 1-hourly coupled model showed good agreements with both satellite-based precipitation and *in situ* radiosonde observations. Thus, a set of sensitivity experiments was carried

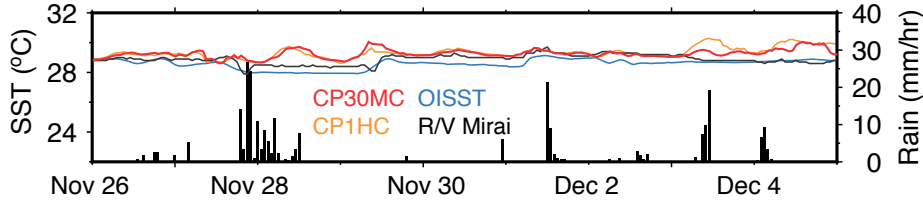


Figure 14. Time series of SSTs simulated/observed during the active phase of the MJO along with the observed precipitation rate by the R/V *Mirai*.

459 out to investigate the impact of the air-sea coupling frequency on convective activities
460 during the MJO.

461 By varying the coupling frequency from 30 minutes to 1 day, we found that the PW
462 in the atmosphere was largely reduced in the barely coupled experiments (12-hourly or
463 daily coupled), associated with the westerly moisture flux anomalies (CP12HC and CP1DC;
464 Figure 4). Our analysis indicated that the occurrences of high RH ($>70\%$) were signif-
465 icantly reduced in the barely coupled experiments, especially at the 500-hPa level (mid-
466 dle troposphere), suggesting that deep convection was suppressed. Such a reduction oc-
467 curred only after the MJO entered its active phase (Figure 6). Similar results were found
468 in the uncoupled (atmosphere-only) model (NOCPC). The analysis of the apparent heat
469 source (Q1) and moisture sink (Q2) budget confirmed that the vertical advection of heat
470 and moisture played the dominant role during the active phase of the MJO, but both
471 were weakened in the barely coupled and uncoupled experiments.

472 According to our results, high-frequency air-sea coupling is necessary for represent-
473 ing the diurnal cycle and the daily mean of SST. Specifically, in 30-minute and 1-hour
474 coupled experiments (CP30MC and CP1HC), the SST successfully reproduced the di-
475 urnal cycle of SST, and the maximum SST appeared at 8:00 UTC, which consisted with
476 observations (Ruppert & Johnson, 2015). However, in CP3HC (CP6HC), the time of the
477 diurnal maximum SST was delayed by 1 hour (3 hours), and such phase lags were also
478 found in surface turbulent heat fluxes (TFLX, Figure 7). The surface air temperature
479 (T2m) and specific humidity (q2m) basically followed the same trend of SST in the highly
480 coupled experiments (with few hours lagged), except in CP6HC where the T2m increased
481 simultaneously with the SST (Figure 7 and 14b). Overall, the SST and TFLX had sim-
482 ilar daily means in the highly coupled experiments but became lower in the barely cou-
483 pled and uncoupled experiments.

484 To evaluate the role of the daily mean SST and its diurnal cycle, we conducted an
485 extra WRF-only experiment (NOCPC++) by using the same daily mean SST from the
486 1-hourly coupled model. The results suggested that the mean SST did play the domi-
487 nant role in promoting convection; however, the higher daytime SST (i.e., the diurnal
488 cycle) also helped in moistening the lower troposphere, which is important for trigger-
489 ing deep convection. As a result, convection was still suppressed in NOCPC++ compared
490 with CP1HC, even with the same daily mean SST.

491 In addition to the modulations in the atmosphere, our study also revealed the role
492 of the coupling frequency in the upper ocean processes. We found that high-frequency
493 air-sea coupling helped the maintenance of shallower mixed and isothermal layers by di-
494 urnal surface heating and cooling, leading to higher surface and upper layer tempera-
495 tures (e.g., Shinoda 2005) and therefore stronger convection.

496 Overall, in comparison with previous studies (e.g., Seo et al., 2014), our study pre-
497 sented more detailed information on the subdaily modulations by the air-sea coupling

498 frequency. Our results demonstrated the critical role of high-frequency coupling in rep-
 499 resenting both diurnal convection and upper ocean features since they were highly cou-
 500 pled with each other. Whats more, although our study focused on one specific MJO event
 501 and covered only two weeks, it is reasonable to consider that the impact of air-sea cou-
 502 pling may become more significant in a long-term simulation/prediction. Thus, further
 503 examination of long-term simulation and other MJO events will be a topic of ongoing
 504 study, together with experiments for resolution dependency (Holloway et al., 2015).

505 Acknowledgments

506 The authors are grateful to all those who engaged in the YMC-Sumatra 2017 field cam-
 507 paign, and the observational dataset is available at (www.jamstec.go.jp/ymc/jpn/ymcj_data.html). We also thank the following institutions/agencies for data provision: Japan
 508 Aerospace Exploration Agency for the GSMaP dataset, the National Centers for Envi-
 509 ronmental Pre-diction for the NCEP-FNL dataset, the National Centers for Environmen-
 510 tal Information for the OISST dataset, the HYbrid Coordinates Ocean Model (HYCOM)
 511 Consortium for Data-Assimilative Ocean Modeling for the GOF3.1 dataset, the U.S.
 512 Geological Survey for the GMTED2010 data, and the Bureau of Meteorology, Australia,
 513 for the RMM MJO index. This numerical experiments in this study were carried out on
 514 the JAMSTEC Super Computer System (DA System).
 515

516 References

- 517 Amante, C., & Eakins, B. (2009). *1 arc-minute global relief model: Procedures,*
 518 *data sources, and analysis (ETOPO1)* [NOAA Technical Memorandum NES-
 519 DIS NGDC-24]. Maryland, United States. (Accessed on 13 May, 2019) doi:
 520 10.7289/V5C8276M
- 521 Bae, S., Hong, S.-Y., & Tao, W. (2018). Development of a single-moment cloud mi-
 522 crophysics scheme with prognostic hail for the weather research and forecasting
 523 (WRF) model. *Asia-Pacific Journal of Atmospheric Sciences*, *55*, 233-245.
 524 doi: 10.1007/s13143-018-0066-3
- 525 Banzon, V., Smith, T. M., Chin, T. M., Liu, C., & Hankins, W. (2016). A long-term
 526 record of blended satellite and in situ sea-surface temperature for climate mon-
 527 itoring, modeling and environmental studies. *Earth System Science Data*, *8*(1),
 528 165-176. doi: 10.5194/essd-8-165-2016
- 529 Chen, X., & Zhang, F. (2019). Relative roles of preconditioning moistening
 530 and global circumnavigating mode on the MJO convective initiation dur-
 531 ing DYNAMO. *Geophysical Research Letters*, *46*(2), 1079-1087. doi:
 532 10.1029/2018GL080987
- 533 Clayson, C. A., & Bogdanoff, A. S. (2013). The effect of diurnal sea surface tem-
 534 perature warming on climatological air-sea fluxes. *Journal of Climate*, *26*(8),
 535 2546-2556. doi: 10.1175/JCLI-D-12-00062.1
- 536 Crueger, T., Stevens, B., & Brokopf, R. (2013). The Madden-Julian oscillation
 537 in ECHAM6 and the introduction of an objective MJO metric. *Journal of Cli-*
 538 *mate*, *26*(10), 3241-3257. doi: 10.1175/JCLI-D-12-00413.1
- 539 Cummings, J. A. (2005). Operational multivariate ocean data assimilation. *Quar-*
 540 *terly Journal of the Royal Meteorological Society*, *131*(613), 3583-3604. doi: 10
 541 .1256/qj.05.105
- 542 Danielson, J. J., & Gesch, D. B. (2011). *Global multi-resolution terrain elevation*
 543 *data 2010 (GMTED2010)* [Open-File Report 20111073]. Virginia, United
 544 States. (Accessed on 13 May, 2019)
- 545 DeMott, C. A., Klingaman, N. P., & Woolnough, S. J. (2015). Atmosphere-ocean
 546 coupled processes in the Madden-Julian oscillation. *Reviews of Geophysics*,
 547 *53*(4), 1099-1154. doi: 10.1002/2014RG000478
- 548 Dipankar, A., Webster, S., Huang, X.-Y., & Doan, V. Q. (2019). Understanding

- 549 biases in simulating the diurnal cycle of convection over the western coast of
 550 Sumatra: Comparison with pre-YMC observation campaign. *Monthly Weather*
 551 *Review*, *147*, 1615-1631. doi: 10.1175/MWR-D-18-0432.1
- 552 Fu, X., Lee, J.-Y., Hsu, P.-C., Taniguchi, H., Wang, B., Wang, W., & Weaver, S.
 553 (2013). Multi-model MJO forecasting during DYNAMO/CINDY period.
 554 *Climate Dynamics*, *41*, 1067-1081. doi: 10.1007/s00382-013-1859-9
- 555 Gerard, L. (2007). An integrated package for subgrid convection, clouds and pre-
 556 cipitation compatible with meso-gamma scales. *Quarterly Journal of the Royal*
 557 *Meteorological Society*, *133*(624), 711-730. doi: 10.1002/qj.58
- 558 Green, B. W., Sun, S., Bleck, R., Benjamin, S. G., & Grell, G. A. (2017). Eval-
 559 uation of MJO predictive skill in multiphysics and multimodel global en-
 560 sembles. *Monthly Weather Review*, *145*(7), 2555-2574. doi: 10.1175/
 561 MWR-D-16-0419.1
- 562 Grell, G. A., & Freitas, S. R. (2014). A scale and aerosol aware stochastic convective
 563 parameterization for weather and air quality modeling. *Atmospheric Chemistry*
 564 *and Physics*, *14*(10), 5233-5250. doi: 10.5194/acp-14-5233-2014
- 565 Hagos, S., Leung, L. R., & Dudhia, J. (2011). Thermodynamics of the Madden-
 566 Julian oscillation in a regional model with constrained moisture. *Journal of the*
 567 *Atmospheric Sciences*, *68*(9), 1974-1989. doi: 10.1175/2011JAS3592.1
- 568 Hagos, S., Zhang, C., Feng, Z., Burleyson, C. D., DeMott, C., Kerns, B., ... Mar-
 569 tini, M. N. (2016). The impact of the diurnal cycle on the propagation
 570 of Madden-Julian oscillation convection across the Maritime Continent.
 571 *Journal of Advances in Modeling Earth Systems*, *8*(4), 1552-1564. doi:
 572 10.1002/2016MS000725
- 573 Holloway, C. E., Woolnough, S. J., & Lister, G. M. S. (2015). The effects of ex-
 574 plicit versus parameterized convection on the MJO in a large-domain high-
 575 resolution tropical case study. part II: Processes leading to differences in MJO
 576 development. *Journal of the Atmospheric Sciences*, *72*(7), 2719-2743. doi:
 577 10.1175/JAS-D-14-0308.1
- 578 Hong, S.-Y., & Jang, J. (2018). Impacts of shallow convection processes on a
 579 simulated boreal summer climatology in a global atmospheric model. *Asia-*
 580 *Pacific Journal of Atmospheric Sciences*, *54*(5), 361-370. doi: 10.1007/
 581 s13143-018-0013-3
- 582 Hong, S.-Y., Noh, Y., & Dudhia, J. (2006). A new vertical diffusion package with an
 583 explicit treatment of entrainment processes. *Monthly Weather Review*, *134*(9),
 584 2318-2341. doi: 10.1175/MWR3199.1
- 585 Iacono, M. J., Delamere, J. S., Mlawer, E. J., Shephard, M. W., Clough, S. A., &
 586 Collins, W. D. (2008). Radiative forcing by long-lived greenhouse gases: Cal-
 587 culations with the AER radiative transfer models. *Journal of Geophysical*
 588 *Research: Atmospheres*, *113*(D13103). doi: 10.1029/2008JD009944
- 589 JAMSTEC, & BPPT. (2018). *Study on air-sea interaction over upwelling region*
 590 *in the eastern Indian Ocean* [R/V Mirai Cruise Report MR17-0]. Retrieved
 591 from [http://www.godac.jamstec.go.jp/catalog/data/doc.catalog/media/
 592 MR17-08_leg1-2_all.pdf](http://www.godac.jamstec.go.jp/catalog/data/doc.catalog/media/MR17-08_leg1-2_all.pdf)
- 593 Jimnez, P. A., Dudhia, J., Gonzalez-Rouco, J. F., Navarro, J., Montvez, J. P.,
 594 & Garca-Bustamante, E. (2012). A revised scheme for the WRF sur-
 595 face layer formulation. *Monthly Weather Review*, *140*(3), 898-918. doi:
 596 10.1175/MWR-D-11-00056.1
- 597 Katsumata, M., Mori, S., Hamada, J.-I., Hattori, M., Syamsudin, F., & Ya-
 598 manaka, M. D. (2018). Diurnal cycle over a coastal area of the Maritime
 599 Continent as derived by special networked soundings over Jakarta during
 600 HARIMAU2010. *Progress in Earth and Planetary Science*, *5*(64). doi:
 601 10.1186/s40645-018-0216-3
- 602 Kayano, M., & Kousky, V. (1999). Intraseasonal (30-60 day) variability in the global
 603 tropics: Principal modes and their evolution. *Tellus A: Dynamic Meteorology*

- 604 *and Oceanography*, 51(3), 373-386. doi: 10.3402/tellusa.v51i3.13459
- 605 Kessler, W. S. (2001). EOF representations of the Madden-Julian oscillation and its
606 connection with ENSO. *Journal of Climate*, 14(13), 3055-3061. doi: 10.1175/
607 1520-0442(2001)014<3055:EROTMJ>2.0.CO;2
- 608 Kim, H., Hoyos, C. D., Webster, P. J., & Kang, I.-S. (2010). Ocean-atmosphere cou-
609 pling and the boreal winter MJO. *Climate Dynamics*, 35, 771-784. doi: 10
610 .1007/s00382-009-0612-x
- 611 Kim, H., Vitart, F., & Waliser, D. E. (2018). Prediction of the Madden-Julian oscil-
612 lation: A review. *Journal of Climate*, 31(23), 9425-9443. doi: 10.1175/JCLI-D
613 -18-0210.1
- 614 Kwon, Y. C., & Hong, S.-Y. (2017). A mass-flux cumulus parameterization scheme
615 across gray-zone resolutions. *Monthly Weather Review*, 145(2), 583-598. doi:
616 10.1175/MWR-D-16-0034.1
- 617 Lorenz, D. J., & Hartmann, D. L. (2006). The effect of the MJO on the
618 North American monsoon. *Journal of Climate*, 19(3), 333-343. doi:
619 10.1175/JCLI3684.1
- 620 Madden, R. A., & Julian, P. R. (1972). Description of global-scale circulation cells
621 in the tropics with a 40-50 day period. *Journal of the Atmospheric Sciences*,
622 29(6), 1109-1123. doi: 10.1175/1520-0469(1972)029<1109:DOGSCC>2.0.CO;2
- 623 Madden, R. A., & Julian, P. R. (2005). Historical perspective. In W. K. M. Lau &
624 D. E. Waliser (Eds.), *Intraseasonal variability in the atmosphere-ocean climate
625 system* (p. 1-16). Springer-Praxis.
- 626 Mishra, S. K., Sahany, S., & Salunke, P. (2017). Linkages between MJO and sum-
627 mer monsoon rainfall over India and surrounding region. *Meteorology and At-
628 mospheric Physics*, 129(6), 283-296. doi: 10.1175/1520-0469(1972)029<1109:
629 DOGSCC>2.0.CO;2
- 630 Morak-Bozzo, S., Merchant, C. J., Kent, E. C., Berry, D. I., & Carella, G. (2016).
631 Climatological diurnal variability in sea surface temperature character-
632 ized from drifting buoy data. *Geoscience Data Journal*, 3(1), 20-28. doi:
633 10.1002/gdj3.35
- 634 Mori, S., Jun-Ichi, H., Tauhid, Y. I., Yamanaka, M. D., Okamoto, N., Murata, F.,
635 ... Sribimawati, T. (2004). Diurnal landsea rainfall peak migration over
636 Sumatera island, Indonesian Maritime Continent, observed by TRMM satel-
637 lite and intensive rawinsonde soundings. *Monthly Weather Review*, 132(8),
638 2021-2039. doi: 10.1175/1520-0493(2004)132<2021:DLRPMO>2.0.CO;2
- 639 Moteki, Q., Katsumata, M., Yoneyama, K., Ando, K., & Hasegawa, T. (2018).
640 Drastic thickening of the barrier layer off the western coast of Sumatra due to
641 the Madden-Julian oscillation passage during the pre-Years of the Maritime
642 Continent campaign. *Progress in Earth and Planetary Science*, 5(35). doi:
643 10.1186/s40645-018-0190-9
- 644 Nasuno, T. (2019). Moisture transport over the western Maritime Continent during
645 the 2015 and 2017 YMC Sumatra campaigns in global cloud-system-resolving
646 simulations. *SOLEA*, 15, 99-106. doi: 10.2151/sola.2019-019
- 647 Nasuno, T., Li, T., & Kikuchi, K. (2015). Moistening processes before
648 the convective initiation of Madden-Julian oscillation events during the
649 CINDY2011/DYNAMO period. *Monthly Weather Review*, 143(2), 622-643.
650 doi: 10.1175/MWR-D-14-00132.1
- 651 NCEP. (2000). *NCEP FNL Operational model global tropospheric analyses, con-
652 tinuing from July 1999*. Boulder CO: Research Data Archive at the National
653 Center for Atmospheric Research, Computational and Information Systems
654 Laboratory. Retrieved from <https://doi.org/10.5065/D6M043C6> (Accessed
655 on 24 May, 2019) doi: 10.5065/D6M043C6
- 656 Neale, R., & Slingo, J. (2003). The Maritime Continent and its role in the global cli-
657 mate: A GCM study. *Journal of Climate*, 16(5), 834-848. doi: 10.1175/1520
658 -0442(2003)016<0834:TMCAIR>2.0.CO;2

- 659 Peatman, S. C., Matthews, A. J., & Stevens, D. P. (2014). Propagation of the
660 Madden-Julian oscillation through the Maritime Continent and scale interac-
661 tion with the diurnal cycle of precipitation. *Quarterly Journal of the Royal*
662 *Meteorological Society*, *140*(680), 814-825. doi: 10.1002/qj.2161
- 663 Pilon, R., Zhang, C., & Dudhia, J. (2016). Roles of deep and shallow convection and
664 microphysics in the MJO simulated by the model for prediction across scales.
665 *Journal of Geophysical Research: Atmospheres*, *121*(18), 10,575-10,600. doi:
666 10.1002/2015JD024697
- 667 Raymond, D. J., & Fuchs, Z. (2009). Moisture modes and the Madden-Julian oscilla-
668 tion. *Journal of Climate*, *22*(11), 3031-3046. doi: 10.1175/2008JCLI2739.1
- 669 Reynolds, R. W., Smith, T. M., Liu, C., Chelton, D. B., Casey, K. S., & Schlax,
670 M. G. (2007). Daily high-resolution-blended analyses for sea surface tempera-
671 ture. *Journal of Climate*, *20*(22), 5473-5496. doi: 10.1175/2007JCLI1824.1
- 672 Ruppert, J. H., & Johnson, R. H. (2015). Diurnally modulated cumulus moist-
673 ening in the preonset stage of the Madden-Julian oscillation during DY-
674 NAMO. *Journal of the Atmospheric Sciences*, *72*(4), 1622-1647. doi:
675 10.1175/JAS-D-14-0218.1
- 676 Seo, H., Subramanian, A. C., Miller, A. J., & Cavanaugh, N. R. (2014). Cou-
677 pled impacts of the diurnal cycle of sea surface temperature on the Madden-
678 Julian oscillation. *Journal of Climate*, *27*(22), 8422-8443. doi: 10.1175/
679 JCLI-D-14-00141.1
- 680 Shinoda, T. (2005). Impact of the diurnal cycle of solar radiation on intraseasonal
681 SST variability in the western Equatorial Pacific. *Journal of Climate*, *18*(14),
682 2628-2636. doi: 10.1175/JCLI3432.1
- 683 Shinoda, T., & Uyeda, H. (2002). Effective factors in the development of deep
684 convective clouds over the wet region of eastern China during the summer
685 monsoon season. *Journal of the Meteorological Society of Japan. Ser. II*,
686 *80*(6), 1395-1414. doi: 10.2151/jmsj.80.1395
- 687 Tewari, M., Chen, F., Wang, W., Dudhia, J., LeMone, M., Mitchell, K., ... Cuenca,
688 R. (2004). *Implementation and verification of the unified NOAA land surface*
689 *model in the WRF model*. Presentation. Seattle, WA, US..
- 690 Tseng, K.-C., Sui, C.-H., & Li, T. (2015). Moistening processes for Madden-Julian
691 oscillations during DYNAMO/CINDY. *Journal of Climate*, *28*(8), 3041-3057.
692 doi: 10.1175/JCLI-D-14-00416.1
- 693 Vitart, F. (2014). Evolution of ECMWF sub-seasonal forecast skill scores. *Quar-*
694 *terly Journal of the Royal Meteorological Society*, *140*(683), 1889-1899. doi: 10
695 .1002/qj.2256
- 696 Waliser, D. E., Lau, K. M., & Kim, J.-H. (1999). The influence of coupled sea
697 surface temperatures on the Madden-Julian oscillation: A model perturba-
698 tion experiment. *Journal of the Atmospheric Sciences*, *56*(3), 333-358. doi:
699 10.1175/1520-0469(1999)056<0333:TIOCSS>2.0.CO;2
- 700 Wang, B., & Moon, J.-Y. (2018). Subseasonal prediction of extreme weather
701 events. In H.-S. Jung & B. Wang (Eds.), *Bridging science and policy im-*
702 *plication for managing climate extremes* (p. 33-48). World Scientific. doi:
703 10.1142/9789813235663_0003
- 704 Warner, J. C., Armstrong, B., He, R., & Zambon, J. B. (2010). Development of
705 a coupled ocean-atmosphere-wave-sediment transport (COAWST) modeling
706 system. *Ocean Modelling*, *35*(3), 230-244. doi: [https://doi.org/10.1016/
707 j.ocemod.2010.07.010](https://doi.org/10.1016/j.ocemod.2010.07.010)
- 708 Webber, B. G. M., Matthews, A. J., & Heywood, K. J. (2010). A dynamical ocean
709 feedback mechanism for the Madden-Julian oscillation. *Quarterly Journal of*
710 *the Royal Meteorological Society*, *136*(648), 740-754. doi: 10.1002/qj.604
- 711 Wu, P., Ardiansyah, D., Mori, S., & Yoneyama, K. (2019, aug). The effect of an
712 active phase of the Madden-Julian oscillation on surface winds over the west-
713 ern coast of Sumatra island. *IOP Conference Series: Earth and Environmental*

- 714 *Science*, 303, 012009. doi: 10.1088/1755-1315/303/1/012009
- 715 Yokoi, S., Mori, S., Katsumata, M., Geng, B., Yasunaga, K., Syamsudin, F., ...
- 716 Yoneyama, K. (2017). Diurnal cycle of precipitation observed in the
- 717 western coastal area of Sumatra island: Offshore preconditioning by grav-
- 718 ity waves. *Monthly Weather Review*, 145(9), 3745-3761. doi: 10.1175/
719 MWR-D-16-0468.1
- 720 Yokoi, S., Mori, S., Syamsudin, F., Haryoko, U., & Geng, B. (2019). Environmental
- 721 conditions for nighttime offshore migration of precipitation area as revealed
- 722 by in situ observation off Sumatra island. *Monthly Weather Review*, 147(9),
723 3391-3407. doi: 10.1175/MWR-D-18-0412.1
- 724 Zermeo-Daz, D. M., Zhang, C., Kollias, P., & Kalesse, H. (2015). The role of shal-
- 725 low cloud moistening in MJO and non-MJO convective events over the ARM
- 726 Manus site. *Journal of the Atmospheric Sciences*, 72(12), 4797-4820. doi:
727 10.1175/JAS-D-14-0322.1
- 728 Zhang, C. (2013). Madden-Julian oscillation: Bridging weather and climate. *Bul-*
729 *letin of the American Meteorological Society*, 94(12), 1849-1870. doi: 10.1175/
730 BAMS-D-12-00026.1
- 731 Zhang, C., & Anderson, S. P. (2003). Sensitivity of intraseasonal perturbations
- 732 in SST to the structure of the MJO. *Journal of the Atmospheric Sciences*,
733 60(17), 2196-2207. doi: 10.1175/1520-0469(2003)060<2196:SOIPIS>2.0.CO;2
- 734 Zhang, C., & Wang, Y. (2017). Projected future changes of tropical cy-
- 735 clone activity over the western North and south Pacific in a 20-km-mesh
- 736 regional climate model. *Journal of Climate*, 30(15), 5923-5941. doi:
737 10.1175/JCLI-D-16-0597.1
- 738 Zheng, Y., Alapaty, K., Herwehe, J. A., Del Genio, A. D., & Niyogi, D. (2016).
- 739 Improving high-resolution weather forecasts using the weather research and
- 740 forecasting (WRF) model with an updated Kain-Fritsch scheme. *Monthly*
741 *Weather Review*, 144(3), 833-860. doi: 10.1175/MWR-D-15-0005.1
- 742 Zhu, J., Wang, W., & Kumar, A. (2017). Simulations of MJO propagation across
- 743 the Maritime Continent: Impacts of SST feedback. *Journal of Climate*, 30(5),
744 1689-1704. doi: 10.1175/JCLI-D-16-0367.1